

1 Identification of Channeling in Pore-Scale Flows

2 **Martina Siena¹, Oleg Iliev², Torben Prill², Monica Riva^{1,3}, and Alberto Guadagnini^{1,3}**

3 ¹Department of Civil and Environmental Engineering, Politecnico di Milano, 20133, Milan, Italy;

4 ²Fraunhofer Institute for Industrial Mathematics, 67663, Kaiserslautern, Germany; ³ Department
5 of Hydrology and Atmospheric Sciences, University of Arizona, Tucson, Arizona 85721, USA.

6 Corresponding author: Martina Siena (martina.siena@polimi.it)

7

8

9 **Key Points:**

- 10 • Fast channels in 3D pore-scale flow fields are identified as connected regions of the pore
11 space where velocity outliers are found.
- 12 • The topology of the network of pore bodies and throats forming the pore space drives
13 spatial distributions of fast channels.
- 14 • Fast channel size decreases as the Reynolds number increases and is related to the
15 strength of preferential flow and anomalous transport.

16

17

18

19

20 **Abstract**

21 We quantify flow channeling at the micro scale in three-dimensional porous media. The
22 study is motivated by the recognition that heterogeneity and connectivity of porous media are key
23 drivers of channeling. While efforts in the characterization of this phenomenon mostly address
24 processes at the continuum scale, it is recognized that pore-scale preferential flow may affect the
25 behavior at larger scales. We consider synthetically-generated pore structures and rely on
26 geometrical/topological features of sub-regions of the pore space where clusters of velocity
27 outliers are found. We relate quantitatively the size of such fast-channels, formed by pore bodies
28 and pore throats, to key indicators of preferential flow and anomalous transport. Pore-space spatial
29 correlation provides information beyond just pore size distribution and drives the occurrence of
30 these velocity structures. The latter occupy a larger fraction of the pore-space volume in pore
31 throats than in pore bodies and shrink with increasing flow Reynolds number.

32 **Plain Language Summary**

33 The movement of fluids and dissolved chemicals through porous media is massively
34 affected by the heterogeneous nature of these systems. The presence of "fast channels", i.e.,
35 preferential flow paths characterized by large velocities persisting over long distances, gives rise
36 to very short solute travel times, with key implications in, e.g., environmental risk assessment.
37 While efforts in the characterization of this phenomenon mostly address processes at the
38 continuum (laboratory or field) scale, it is recognized that pore-scale channeling of flow may affect
39 the system behavior at larger scales. Here, we provide criteria for the identification of fast channels
40 at the pore scale, addressing feedback between channeling and geometrical/topological features of
41 the investigated porous structures. Our results clearly evidence the major role of well-defined
42 regions in the pore space, termed pore throats, in driving flow channeling. We also find that the
43 strength of channeling is controlled by the characteristic Reynolds number of the flow field.

44 **1. Introduction**

45 Predictions of flow and transport processes in porous media are critically affected by the
46 heterogeneous nature of pore spaces, intrinsically characterized by irregular geometrical features
47 and properties that can vary widely across multiple spatial scales (Neuman, 2008; Neuman & Di
48 Federico, 2003; Zami-Pierre et al., 2016). Notably, flow and transport phenomena are affected not
49 only by the degree of heterogeneity of the medium, but also by the spatial arrangement of its
50 hydraulic properties, a prominent role being played by connectivity (Knudby & Carrera, 2005).
51 While being seen as quite intuitive, the concept of connectivity is still lacking a formal and
52 unambiguous definition. It can be regarded as a measure of the presence of preferential flow paths
53 (or *fast channels*) across which flow tends to focus and be associated with high velocity values.
54 Understanding the mechanisms driving flow to concentrate in high-velocity channels is key for
55 proper prediction of first arrival times of dissolved chemicals at critical targets (Nissan &
56 Berkowitz, 2018; Tartakovsky & Neuman, 2008; Zinn & Harvey, 2003) and the characterization
57 of multiphase flow processes (Dai & Santamarina, 2013; Jiménez-Martínez et al., 2015), with
58 direct implications in several settings, including, e.g., environmental risk assessment or enhanced
59 oil recovery. Channeling may occur under diverse conditions and on a wide range of spatial scales,
60 and is always characterized by two major features: (i) high velocity values persisting over long
61 distances; and (ii) flow focused within a few regions (principal paths) of the pore space (Hyman
62 et al., 2012; Le Goc et al., 2010). Metrics suggested to quantify connectivity (Renard & Allard,
63 2013) are typically related to scenarios at the continuum (Darcy or field) scale and rely on the

64 identification of connected paths of hydraulic properties (Dell’Arciprete et al., 2014; Le Goc et al.,
65 2010) or of high-velocity patterns along flow trajectories (Fiori & Jankovic, 2012). While some
66 indication about the level of channeling at the Darcy scale can be gained by the correlation length
67 of permeabilities, this is not the case at the pore scale. Characterization of channeling for two-
68 dimensional geometries is presented in Alim et al. (2017) relying on the pore network method, and
69 in Nissan & Berkowitz (2018) solving Navier-Stokes equations for given pore geometries. Time
70 evolution of the statistics of experimental observations of Lagrangian velocities in three-
71 dimensional porous samples are analyzed in Carrel et al. (2018) to evaluate the effect of
72 progressive biofilm growth on flow channeling.

73 In this Letter we propose a procedure to characterize quantitatively channeling phenomena
74 at the pore level for three-dimensional voxelized geometries. This is achieved by (i) mapping the
75 (continuous) velocity field into a categorical variable and (ii) studying geometrical and topological
76 properties of the sub-regions of pore space associated with a given velocity class. The effectiveness
77 of the approach proposed here is supported by the observation that our criteria lead to the
78 quantification of a degree of channeling that is consistent with the magnitude of effects that
79 channeling can have on flow and transport patterns documented at the continuum scale, resulting
80 in preferential flow and anomalous transport (Bijeljic et al., 2011; De Anna et al., 2013; Kang et
81 al., 2014 and reference therein).

82 2. Materials and Methods

83 2.1 Synthetic pore structure generation

84 Let ξ [-] be a (dimensionless) measure of channeling. The latter can be related to main
85 governing quantities through the following functional form

$$86 \quad \xi = f(\rho, \mu, V, L, \phi, \text{pdf}_R) \quad (1)$$

87 where ρ [M L^{-3}] and μ [$\text{M L}^{-1} \text{T}^{-1}$] are fluid density and viscosity, respectively, V [L T^{-1}] is a
88 characteristic velocity, L [L] represents the length size of (porous) domain, ϕ [-] is the sample
89 porosity, and pdf_R is the probability density function of the pore size, R [L]. We study ξ on
90 synthetically-generated, isotropic three-dimensional pore structures obtained on regular cubic
91 grids from the convolution of a uniform distribution on $[0,1]$ with a symmetric Gaussian kernel of
92 width σ (Hyman & Winter, 2014). A binary image is obtained by allocating each cell of the grid
93 either to the pore space or to the solid matrix, according to a level threshold $\gamma \in (0,1)$ applied to
94 the generated random field. Let Ω_{pore} be the subset of grid cells that are associated with the pore
95 space. Two cells in Ω_{pore} , identified by the coordinates of their centers (\mathbf{x}_A and \mathbf{x}_B), are said to
96 be connected if there exists a sequence of neighboring cells (i.e., of cells sharing a face) completely
97 included in Ω_{pore} and linking \mathbf{x}_A to \mathbf{x}_B . A group of connected cells is termed a *cluster*. For all
98 blocks considered, the generation algorithm renders pore spaces exhibiting one dominant cluster.
99 The final pore structures are obtained by removing all cells in Ω_{pore} that are not connected to the
100 main cluster. It can be shown (Siena et al., 2014) that the two generation parameters, γ and σ ,
101 control porosity, ϕ , and mean pore size, $\langle R \rangle$, of the sample, respectively. The spatial correlation
102 of the void space depends on both γ and σ . A key feature of the selected generator is that it allows

103 reproducing sample pdf_R displaying exponential positive tails, the latter being consistently
 104 observed in samples of real porous systems (Holzner et al., 2015; Lindquist et al., 2000). Assuming
 105 that pdf_R can be approximated by an exponential distribution, equation (1) can be written in
 106 dimensionless form as

$$107 \quad \xi = \bar{f} \left(\text{Re}, \phi, \frac{\langle R \rangle}{L} \right) \quad (2)$$

108 $\text{Re} = \rho V \langle R \rangle / \mu$ being the flow Reynolds number. In this Letter, we aim at assessing the impact of
 109 Re and $\langle R \rangle / L$, on the channeling metric ξ .

110 We generate three sets of cubic blocks, hereafter termed as set 1, 2, and 3, each comprising
 111 a collection of 10 realizations. We set $L = 1.28$ cm, a voxel number $N = 128^3$ (i.e., voxel size
 112 $dl = 100 \mu\text{m}$), $\gamma = 0.45$ (which provided $\phi \approx \text{const} = 0.4$) and we vary σ as 0.01, 0.03 or 0.05,
 113 for set 1, 2, and 3, respectively. Figures 1a-1c depict cross-sectional contours of the inner structure
 114 of a representative block, termed as B_1 , B_2 and B_3 , from each of these sets.

115 2.2 Synthetic pore structure topology

116 Geometrical and topological properties of the synthetic pore structures are inferred through
 117 a maximal ball (MB) algorithm. Amongst all spheres that are subsets of the pore space volume,
 118 MBs are those that are not fully contained in any other sphere. The pore-space skeleton can hence
 119 be identified as the set of points in the pore space that are centers of a MB (Silin & Patzek, 2006).
 120 The size R of a pore is then evaluated at each point of the pore-space skeleton as the radius of the
 121 largest sphere inscribed in the void space, measured by means of an inflating-deflating algorithm
 122 (Dong & Blunt, 2009). The (dimensionless) mean pore sizes, $\langle R \rangle / L$, of the three blocks depicted
 123 in Figures 1a-1c are 0.012, 0.036, and 0.050, respectively for B_1 , B_2 , and B_3 (with averages of
 124 0.011, 0.032, and 0.047 across block sets 1, 2, and 3). The MB algorithm also allows classifying
 125 each sphere according to a given type of topological element, i.e., pore body (PB) or pore throat
 126 (PT) (Dong & Blunt, 2009). Following this approach, each voxel in the void space is associated
 127 with a given pore size, R , and with the corresponding topological class.

128 2.3 Flow simulations

129 We perform direct numerical simulations of steady-state, single-phase, fully-saturated flow
 130 throughout the pore space of the generated blocks. We rely on the widely tested software GeoDict
 131 (Math2Market GmbH) by setting (i) the mean velocity, V , at the inlet, $z = 0$, (ii) a constant pressure
 132 at the outlet, $z = L$, and (iii) impermeable lateral boundaries. GeoDict implements a finite volume
 133 scheme to solve the Navier-Stokes equations, combining a SIMPLE algorithm with a Fast Fourier
 134 Transform approach to speed up the solution of the Poisson equation for pressure. Values of V at
 135 the inlet are set to obtain two diverse values of the Reynolds number for each block, i.e., $\text{Re} = 0.1$,
 136 10. Within this range of Re , Nissan & Berkowitz (2018) documented a transition from linear
 137 (Darcy) flow to nonlinear behavior in two-dimensional porous media.

138 3. Results and discussion

139 3.1 Velocity clusters

140 For ease of illustration, we focus here on results obtained in B_1 , B_2 and B_3 . Outcomes of
 141 similar quality are obtained for all of the blocks generated.

142 Histograms and box plots of (normalized) computed velocities, $v_N = |\mathbf{v}|/V$, $|\mathbf{v}|$ being the
 143 norm of the local velocity vector \mathbf{v} , obtained in B_1 , B_2 and B_3 are depicted in Figures 1d, 1e and 1f,
 144 respectively, for $Re = 0.1$ and in Figures 1g, 1h and 1i for $Re = 10$. All plots are indicative of a
 145 common behavior of the computed velocity distributions, which are markedly right skewed, i.e.,
 146 skewed toward large values, for $Re = 0.1$. An increase of Re causes the extent of the support of the
 147 sample pdf of v_N to decrease, resulting in a more homogeneous flow field, a feature also observed
 148 by Nissan & Berkowitz (2018). These results are complemented by Figures S1 and S2 in the
 149 supporting information, depicting histograms of v_N values sampled in PBs and PTs.

150 We quantify channeling by introducing a categorical variable, $i = 1, \dots, 5$. The latter is
 151 assigned to each voxel of the pore-space volume, Ω_{pore} , according to: $i = 1$ if $0 \leq v_N < Q_1$; $i = 2$ if
 152 $Q_1 \leq v_N < Q_2$; $i = 3$ if $Q_2 \leq v_N < Q_3$; $i = 4$ if $Q_3 \leq v_N < (Q_3 + 1.5IQR)$; and $i = 5$ if
 153 $v_N \geq (Q_3 + 1.5IQR)$, where $IQR = Q_3 - Q_1$ is the interquartile range, Q_1 , Q_2 , and Q_3 respectively
 154 denoting the quartiles of the ranked set of v_N values. Note that, according to Tukey (1977), all
 155 values of a distribution which are larger than $Q_3 + 1.5 IQR$ are regarded as mild outliers. The sub-
 156 region of the pore space occupied by the categorical variable i is denoted as Ω_i . The study of
 157 clusters within Ω_i is aimed at identifying objects displaying the main features of channeling (i.e.,
 158 large velocities which persist over long distances and are concentrated along only a few pathways)
 159 that are then used for a quantitative evaluation of these phenomena. We note that Ω_i becomes less
 160 fragmented (i.e., the total number of distinct clusters forming Ω_i decreases) as i increases, for all
 161 media and for both values of Re considered (see Tables S1 and S2 in the supporting information).
 162 The mean cluster size shows a maximum for $i = 4$, a class which essentially contains one dominant
 163 cluster.

164 The connectivity function, $\tau_i^j(h)$, of category $i = 1, \dots, 5$, along direction $j = \{x, y, z\}$,
 165 represents the probability that two cells in the same category and separated by a given distance are
 166 connected. According to Renard & Allard (2013), $\tau_i^j(h)$ can be computed as:

$$167 \tau_i^j(h) = \frac{N(\mathbf{x}_A \leftrightarrow \mathbf{x}_B | \mathbf{x}_A \in \Omega_i, \mathbf{x}_B \in \Omega_i, \mathbf{x}_A - \mathbf{x}_B = h\mathbf{e}_j)}{N(\mathbf{x}_A \in \Omega_i, \mathbf{x}_B \in \Omega_i, \mathbf{x}_A - \mathbf{x}_B = h\mathbf{e}_j)} \quad (3)$$

168 where the denominator $N(\mathbf{x}_A \in \Omega_i, \mathbf{x}_B \in \Omega_i, \mathbf{x}_A - \mathbf{x}_B = h\mathbf{e}_j)$ indicates the number of pairs of cells
 169 (identified by their centroids $(\mathbf{x}_A, \mathbf{x}_B)$) belonging to category i that are separated by a distance h
 170 along direction j (as represented by the unit vector \mathbf{e}_j). The numerator in equation (3)
 171 $N(\mathbf{x}_A \leftrightarrow \mathbf{x}_B | \mathbf{x}_A \in \Omega_i, \mathbf{x}_B \in \Omega_i, \mathbf{x}_A - \mathbf{x}_B = h\mathbf{e}_j)$ is the number of these pairs that also belong to the

172 same cluster. Figure 2 collects graphical depictions of $\tau_i^j(h)$ in blocks B_1 (Figures 2a - 2c), B_2
 173 (Figures 2d - 2f) and B_3 (Figures 2g - 2i) for $\text{Re} = 0.1$. The largest separation distance h over which
 174 $\tau_i^j > 0$ provides a measure of the maximum extent of a single cluster of category i along direction
 175 j , $\ell_M^{i,j}$. We note that $\ell_M^{i,j}$ is roughly isotropic (i.e., it does not change with j) for classes $i = 1, \dots, 4$
 176 in all blocks considered. Class $i = 4$ in B_1 and classes $i = 2, 3, 4$ in both B_2 and B_3 have clusters
 177 spanning almost the whole extent of the block ($\ell_M^{i,j} \approx L$). Close inspection of these classes reveals
 178 that these are essentially formed by a dominant cluster (with total size larger than 75% of the
 179 corresponding Ω_i) percolating in all directions, both parallel and normal to the mean flow
 180 direction, z . Such clusters are spread over the whole domain and are not concentrated within a few
 181 areas. Hence, they cannot be regarded as representative to quantify channeling. Otherwise, class i
 182 $= 5$ of v_N outliers exhibits a clear anisotropic behavior: the largest distance encompassed by a
 183 cluster in Ω_5 along the mean flow direction, $\ell_M^{5,z}$, is larger than its counterparts evaluated along
 184 the transverse directions x and y , $\ell_M^{5,x}$ and $\ell_M^{5,y}$ being less than 25% of the total block size. These
 185 features documented for τ_5^j support the choice of clusters associated with v_N outliers as a
 186 grounding element for the characterization of channeling. Comparing the results obtained for the
 187 three porous systems studied, it can be noted that τ_5^j shows a near-stepwise behavior in B_2 (Figures
 188 2d - 2f) and B_3 (Figures 2g - 2i), sharply dropping to 0 from values ≈ 1 . Otherwise, values of τ_5^j
 189 in B_1 decreases smoothly with h , assuming values in the whole range $[0, 1]$. These results are
 190 indicative of a more fragmented Ω_5 domain in B_1 , with generally more limited maximum lengths,
 191 $\ell_M^{5,j}$, as compared to B_2 and B_3 . The most relevant effect of increasing Re is to reduce $\ell_M^{5,j}$ in all
 192 directions (see Figure S3 in the supporting information).

193 3.2 Characterization of fast channels

194 We expect the relevance of channeling effects to be enhanced when high-velocity clusters
 195 are associated with enhanced persistence (i.e., in term of their elongation in the mean flow
 196 direction). We evaluate the cumulative distribution (*cdf*) of the longitudinal extent of clusters of
 197 velocity outliers, $\ell^{5,z}$, to identify the value of $\ell^{5,z}$ that corresponds to the 95th percentile of such a
 198 distribution. We regard as fast channels all clusters in Ω_5 having a longitudinal extent larger than
 199 this threshold, which corresponds to $L/2$ for B_2 and B_3 and to $L/3$ for B_1 . Figures 3a and 3c depict
 200 the spatial pattern of the only cluster that fulfills this condition within block B_3 , respectively for
 201 $\text{Re} = 0.1$ and $\text{Re} = 10$. Note that each cell of the cluster is colored according to the associated type
 202 of topological element. The cluster encompasses both PBs and PTs, the large majority of the cluster
 203 volume being associated with PTs (green cells). A qualitative comparison between Figures 3a and
 204 3c reveals that the cluster tends to shrink with increasing Re . This result is consistent with the
 205 findings of Nissan & Berkowitz (2018), where it is shown that an increase of Re is associated with
 206 an increased homogeneity of the flow field which, in turn, leads to a smaller amount of velocity
 207 outliers and, hence, a reduction of fast channel volume. An accurate characterization of the size of
 208 the above identified cluster in Ω_5 can be obtained by application of the MB algorithm to its
 209 skeleton, to then evaluate the MB-based radius, R_5 , associated with each point in the cluster. To

210 investigate the relationship between Ω_5 clusters and the geometry/topology of the pore structures
 211 analyzed, we evaluate the ratio between R_5 and R within Ω_5 . Since each cell is labeled according
 212 to the associated type of topological element, R_5/R can be computed separately for PB and PT.
 213 Figures 3b and 3d depict sample probability distribution functions (PDFs) of R_5/R , respectively
 214 for $Re = 0.1$ and $Re = 10$. In both plots, one can clearly note that the support of the PDF in PTs
 215 (green bars) is wider and shifted toward larger values than the one of its PB counterparts (red bars).
 216 These findings suggest that the relative fraction of PT volume occupied by velocity outliers tends
 217 to be larger than its counterpart related to PBs. Similar results (see supporting information, Figures
 218 S4 and S5) have been obtained for block B_2 and, to a limited extent, for block B_1 .

219 3.3 Channeling effects on flow and transport

220 To further support the ability of our criteria to identify channeling, we investigate links
 221 between the definition of fast channels introduced here and metrics typically employed to assess
 222 flow and transport features at the continuum scale. These include, e.g., (i) the degree of preferential
 223 flow, as quantified by the participation number (Andrade et al., 1999; Nissan & Berkowitz, 2018),
 224 and (ii) deviations from Fickian transport behavior.

225 We follow Andrade et al. (1999) and Nissan & Berkowitz (2018) and consider the
 226 participation number as $\pi = \left(n \sum_{i=1}^n q_i^2 \right)^{-1}$ (n is the total number of cells discretizing the pore space;
 227 $q_i = e_i / \sum_{j=1}^n e_j$; and $e_i = u_i^2 + v_i^2 + w_i^2$ is representative of the kinetic energy of a given cell; $u_i, v_i,$
 228 and w_i being the velocity components along x, y and z axis, respectively). The kinetic energy is
 229 constant in all cells (i.e., $\pi = 1$) for a perfectly homogeneous flow. As preferential flow becomes
 230 more pronounced, π decreases. We evaluate this quantity in each flow field with $Re = 0.1$ and
 231 obtain $\bar{\pi} = 0.22, 0.16$ and 0.15 for set 1, 2 and 3, respectively, the overbar representing the average
 232 over 10 realizations. These values indicate that set 2 and set 3 are characterized by a more
 233 pronounced preferential flow than set 1.

234 We also simulate transport of a passive chemical through an advective particle tracking
 235 approach (Russian et al., 2016) following injection of $N_P = 10^4$ particles uniformly distributed at
 236 the block inlet in each Eulerian steady-state flow field. We measure the average solute spreading
 237 in terms of centered mean squared displacement (MSD) along the main flow direction,
 238 $MSD_z(t) = \sum_{i=1}^{N_P} [z_i(t) - \mu_z(t)]^2 / N_P$, where $\mu_z(t) = \sum_{i=1}^{N_P} z_i(t) / N_P$, and distribution of first passage
 239 times ($FPT = \tau$), i.e., the time required to a particle to reach the block outlet. Figure 4a depicts
 240 the temporal evolution of MSD_z obtained for $Re = 0.1$ by averaging over each set of 10 realizations
 241 (solid thick curves). All of these curves exhibit an asymptotic power-law scaling (with trend $\propto t^\alpha$
 242) that deviates from the Fickian trend ($\propto t$, dashed thick lines). Estimates of the scaling exponent
 243 are $\alpha = 1.39, 1.49,$ and 1.80 for set 1, 2, and 3, respectively, indicating a more super-diffusive
 244 behavior in the latter. Figure 4b depicts the density distribution of first passage times, $f(\tau)$,
 245 obtained by considering all of the particles for each set of 10 realizations. The right tail is
 246 characterized by a power-law decay (with slope $\propto t^{-1-\beta}$) for all distributions, with $\beta = 1.98, 1.58$
 247 and 1.10 , for set 1, 2 and 3, respectively. Note that the distribution of particle arrival times tends
 248 to broaden with decreasing β . These results further support the observation of a higher degree of

249 anomalous transport behavior for set 3. Figure 4 also shows that the scaling behavior exhibited by
250 MSD_z and $f(\tau)$ in each single realization (dotted thin curves) is very close to the one observed
251 from the average over the whole set.

252 A clear connection between our proposed definition of fast channels (i.e., clusters in Ω_5
253 associated with values of $\ell^{5,z}$ above the 95th percentile of the corresponding distribution) and the
254 occurrence of anomalous transport is offered by Figure 4c. The latter depicts the fast channel
255 identified in block B_3 for $Re = 0.1$, together with the trajectories of all injected particles over a
256 time range of $3t_{adv}$, where $t_{adv} = \langle R \rangle / V$. The lowest FPT evaluated for the system is equal to $2t_{adv}$
257 (not shown). The fast channel depicted in Figure 4c and identified according to our criteria is the
258 portion of the pore space where particles with $FPTs \leq 3t_{adv}$ tend to focus. As such, it is the main
259 driver of the heterogeneous longitudinal spreading of solute particles that could be inferred from
260 the MSD_z and $f(\tau)$ curves.

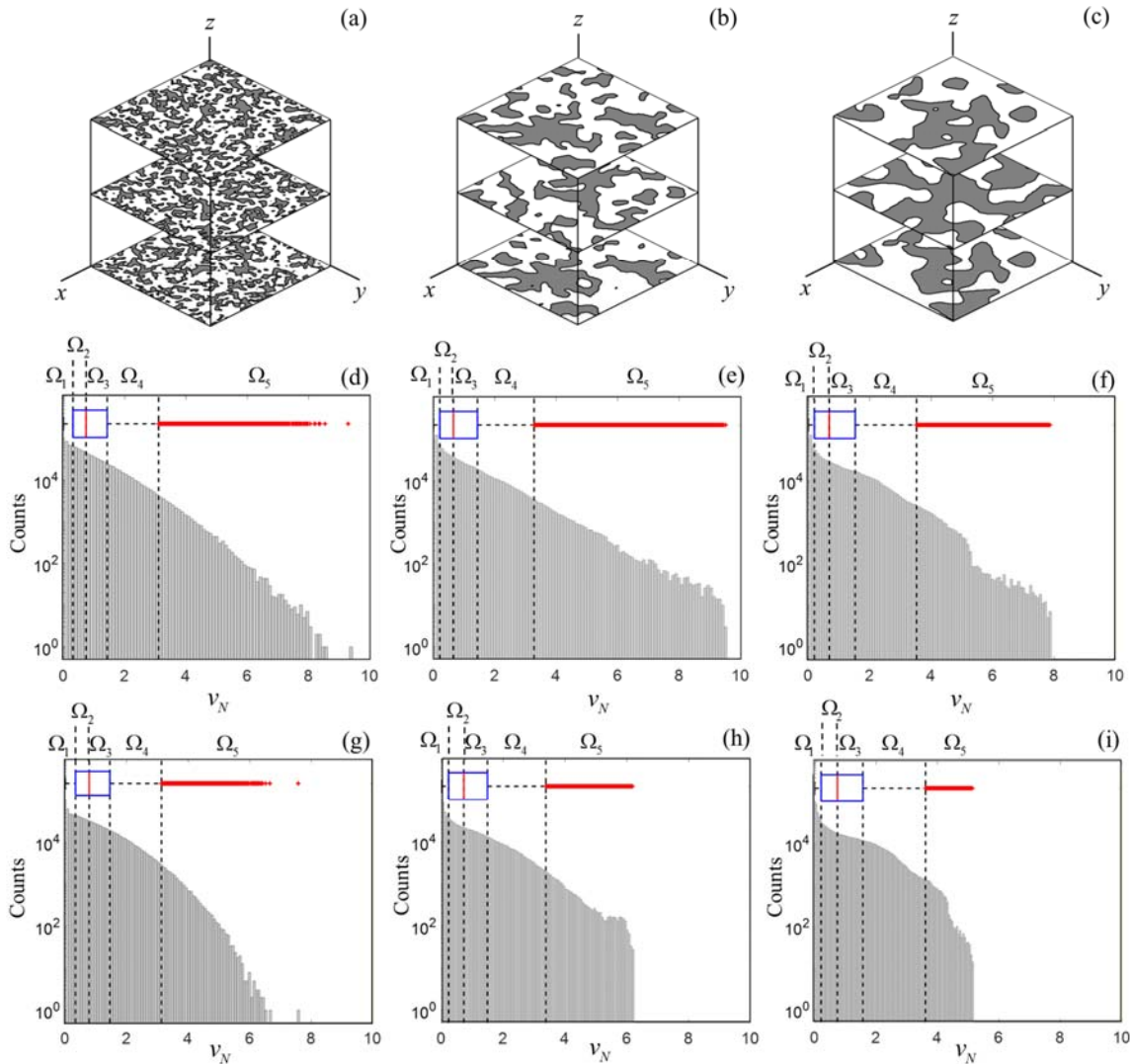
261 We quantify flow channeling by means of volumetric size ($\xi_1 = \overline{W_{FC}}$) and longitudinal
262 extent ($\xi_2 = \overline{\ell^{FC,z}}$) of fast-channels, averaged over each set of 10 realizations. A quantitative
263 relationship between the degree of preferential flow, anomalous transport and our definition of fast
264 channels can be inferred by comparing the participation number, $\bar{\pi}$, and the scaling exponents α
265 and β with $\overline{W_{FC}}$ and $\overline{\ell^{FC,z}}$. For $Re = 0.1$, we obtain $\overline{W_{FC}} = 915, 10330$ and 27122 voxels and
266 $\overline{\ell^{FC,z}} = 56, 91$ and $100 dl$, for set 1, 2, and 3, respectively. This result indicates that set 1, which
267 is characterized by a more homogeneous flow pattern and by a less anomalous transport behavior,
268 has a considerably smaller extent of fast channels with respect to sets 2 and 3.

269 All of these findings indicate that our definition of fast channels is directly related to
270 continuum-scale features of flow and transport processes. We find analogous results considering
271 the three sets of porous blocks for $Re = 10$. Further to this, as observed in Section 3.2, fast channels
272 tend to shrink along all directions as the flow Reynolds number increases in each set of pore
273 structures (with $\overline{W_{FC}} = 406, 6309, 15384$ voxels and $\overline{\ell^{FC,z}} = 42, 82, 83 dl$). This behavior is
274 consistent with the occurrence of increasingly homogeneous flow fields (as indicated by $\bar{\pi} = 0.27,$
275 $0.22, 0.19$) and decreased anomalous transport behavior ($\alpha = 1.37, 1.40, 1.78$; $\beta = 2.8, 1.79,$
276 1.42), as compared against the scenarios for $Re = 0.1$.

277 4. Conclusions

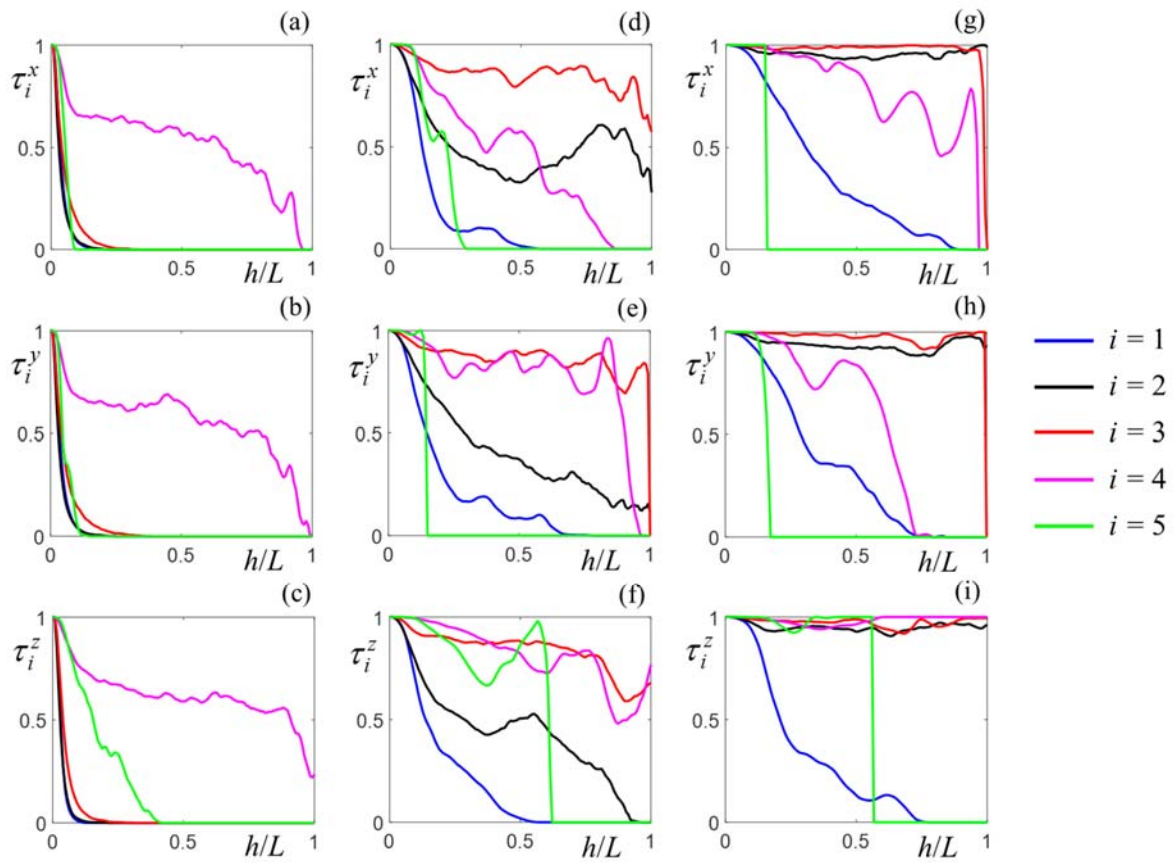
278 In this Letter we propose formal criteria for the quantitative assessment of channeling
279 phenomena at the pore level in three-dimensional voxelized synthetic pore structures. Key results
280 of our study can be summarized as follows: (i) clusters of velocity outliers can be identified with
281 fast channels, i.e., preferential pathways/channels of flow and this analogy enables us to delineate
282 fast channels with a well-defined geometry; (ii) as the pore-space spatial correlation increases, the
283 size of fast channels increases; (iii) fast channels tend to shrink along all directions as the flow
284 Reynolds number increases; (iv) fast channels tend to occupy a larger fraction of the pore-space
285 volume in PTs than they do in PBs; (v) fast channels size can be related quantitatively to the degree
286 of preferential flow and anomalous transport associated with a continuum-scale depiction of the
287 system. These findings will serve as the basis for further investigation on a wider spectrum of pore-

288 space models, aimed at identifying accurate statistically-based geometrical and/or topological
 289 signatures of channeling phenomena.



290
 291 Figure 1. Top: Cross-sectional contours of the pore space (grey areas) in B_1 (a), B_2 (b), and B_3 (c).
 292 Bottom: Histograms of normalized velocity values, v_N , obtained in B_1 , B_2 and B_3 for $Re = 0.1$ (1d-
 293 1f) and for $Re = 10$ (1g-1i). Box plots of v_N are also depicted to represent the thresholds used to
 294 define velocity classes (dashed lines).

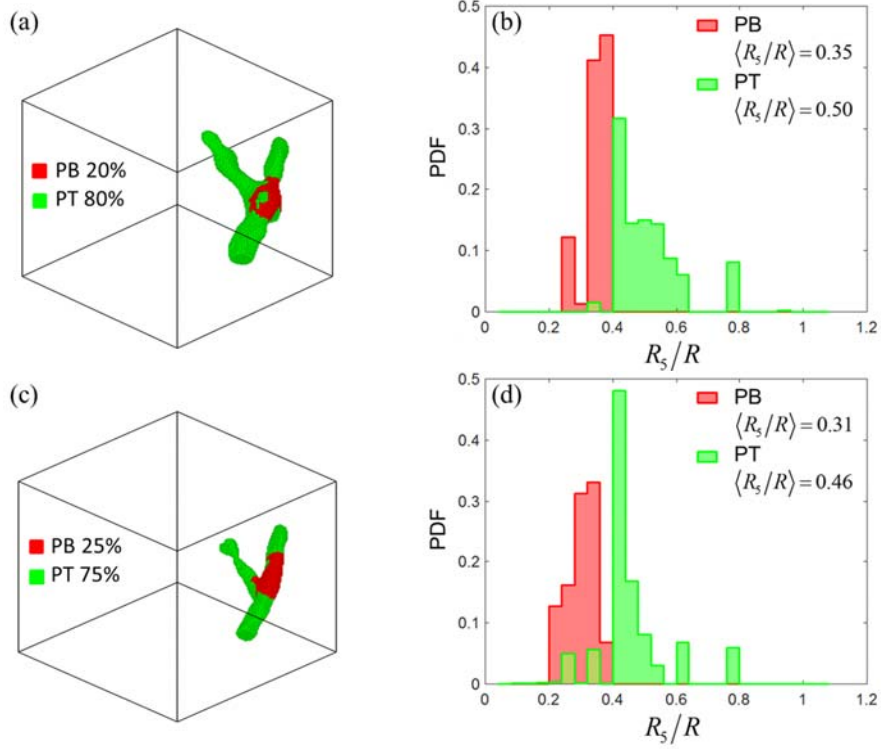
295



296
 297 Figure 2. Connectivity function τ_i^j obtained for each velocity class ($i = 1, \dots, 5$) along directions
 298 $j = x, y, z$, in B_1 (a-c), B_2 (d-f), and B_3 (g-i) for $Re = 0.1$.

299

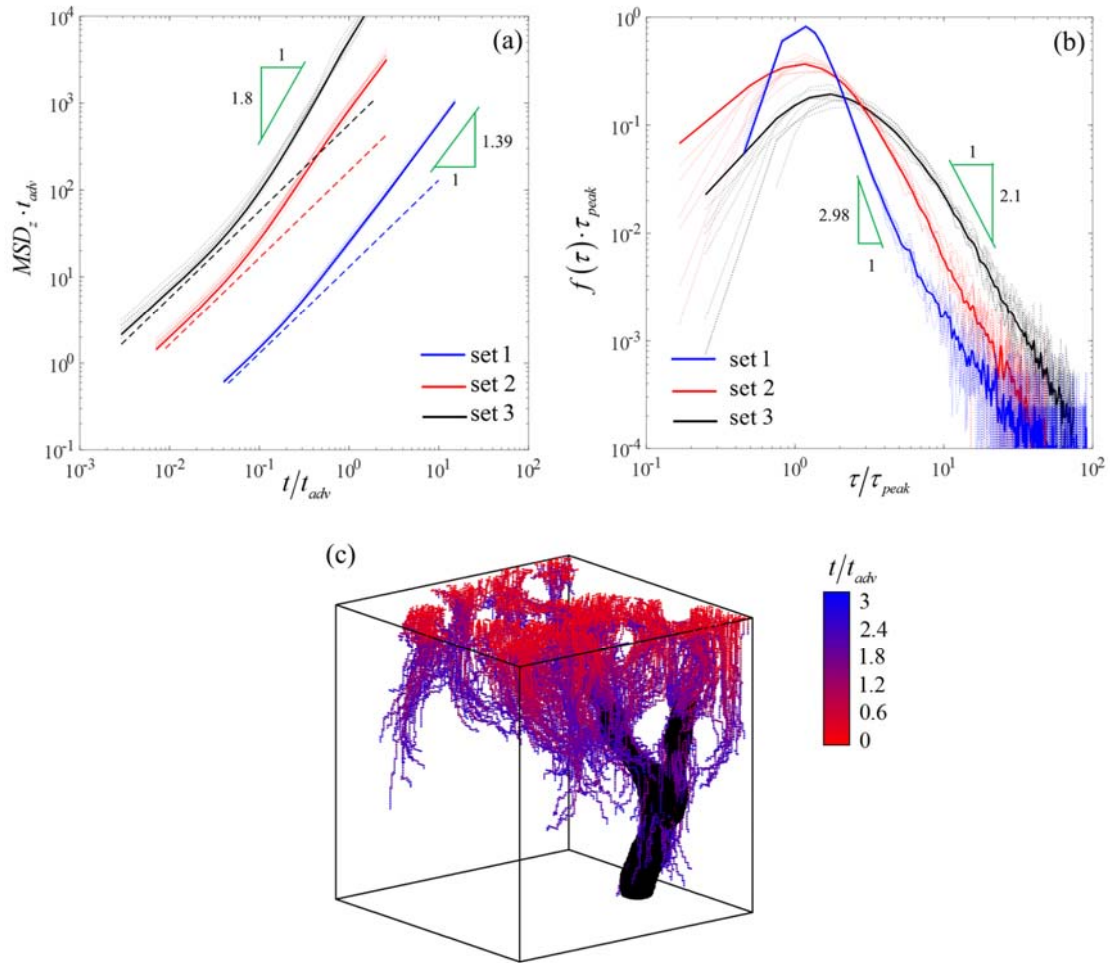
300



301

302 Figure 3. Block B_3 : Left: representation of the Ω_5 cluster having $\ell^{5,z}$ above the 95th percentile for
 303 (a) $Re = 0.1$ and (c) $Re = 10$. Voxels belonging to PBs and PTs are respectively depicted in red
 304 and green. Right: PDF of R_5/R evaluated in the selected Ω_5 cluster for PBs (red bars) and PTs
 305 (green bars) for (b) $Re = 0.1$ and (d) $Re = 10$.

306



307
 308 Figure 4. (a) Temporal evolution of the centered mean squared displacement along the z -axis
 309 (MSD_z) averaged across the 10 realizations of set 1, 2 and 3. Dashed lines correspond to Fickian
 310 behavior ($\propto t$). Results obtained for each pore-space realization are depicted (dotted curves). Time
 311 is rescaled by the advective travel time, t_{adv} . (b) First passage time distribution, $f(\tau)$, obtained by
 312 considering all particles in the 10 realizations for each block set. Results corresponding to each
 313 single realization are depicted (dotted curves). $FPTs$ are rescaled by τ_{peak} , i.e., the FPT at which
 314 the distribution peak is attained. (c) Fast channel (black volume) in B_3 for $Re = 0.1$ and associated
 315 particle trajectories (dotted curves) over a time range of $3t_{adv}$. Colors represent (normalized) times
 316 at which a given position is reached.
 317

318 Acknowledgments

319 This work was supported by the Fraunhofer Award for Young Researchers, established by
 320 the International Society for Porous Media, InterPore, in cooperation with the Fraunhofer institute
 321 for Industrial Mathematics, ITWM (Kaiserslautern). The data are available at
 322 [https://data.mendeley.com/datasets/mbzzyxc2cf/draft?a=68bfb0b3-5478-4eb6-bbe1-](https://data.mendeley.com/datasets/mbzzyxc2cf/draft?a=68bfb0b3-5478-4eb6-bbe1-431ce6904575)
 323 [431ce6904575](https://data.mendeley.com/datasets/mbzzyxc2cf/draft?a=68bfb0b3-5478-4eb6-bbe1-431ce6904575).

324 **References**

- 325 Alim, K., Parsa, S., Weitz, D. A., & Brenner, M. P. (2017). Local Pore Size Correlations Determine
326 Flow Distributions in Porous Media. *Physical Review Letters*, *119*(14), 144501.
327 <https://doi.org/10.1103/PhysRevLett.119.144501>.
- 328 Andrade, J. S., Costa, U. M. S., Almeida, M. P., Makse, H. A., & Stanley, H. E. (1999). Inertial
329 effects on fluid flow through disordered porous media. *Physical Review Letters*, *86*(26),
330 5249. <https://doi.org/10.1103/PhysRevLett.82.5249>.
- 331 Bijeljic, B., Mostaghimi, P., & Blunt, M. J. (2011). Signature of non-Fickian solute transport in
332 complex heterogeneous porous media. *Physical Review Letters*, *107*(20), 204502.
333 <https://doi.org/10.1103/PhysRevLett.107.204502>.
- 334 Carrel, M., Morales, V. L., Dentz, M., Derlon, N., Morgenroth, E., & Holzner, M. (2018). Pore-
335 Scale Hydrodynamics in a Progressively Bioclogged Three-Dimensional Porous Medium: 3-
336 D Particle Tracking Experiments and Stochastic Transport Modeling. *Water Resources*
337 *Research*, *54*(3), 2183–2198. <https://doi.org/10.1002/2017WR021726>.
- 338 Dai, S., & Santamarina, J. C. (2013). Water retention curve for hydrate-bearing sediments.
339 *Geophysical Research Letters*, *40*(21), 5637–5641. <https://doi.org/10.1002/2013GL057884>.
- 340 De Anna, P., Le Borgne, T., Dentz, M., Tartakovsky, A. M., Bolster, D., & Davy, P. (2013). Flow
341 intermittency, dispersion, and correlated continuous time random walks in porous media.
342 *Physical Review Letters*, *110*(18), 184502. <https://doi.org/10.1103/PhysRevLett.110.184502>.
- 343 Dell’Arciprete, D., Vassena, C., Baratelli, F., Giudici, M., Bersezio, R., & Felletti, F. (2014).
344 Connectivity and single/dual domain transport models: tests on a point-bar/channel aquifer
345 analogue. *Hydrogeology Journal*, *22*(4), 761–778. [https://doi.org/10.1007/s10040-014-1105-](https://doi.org/10.1007/s10040-014-1105-5)
346 [5](https://doi.org/10.1007/s10040-014-1105-5).
- 347 Dong, H., & Blunt, M. J. (2009). Pore-network extraction from micro-computerized-tomography
348 images. *Physical Review E*, *80*(3), 036307. <https://doi.org/10.1103/PhysRevE.80.036307>.
- 349 Fiori, A., & Jankovic, I. (2012). On Preferential Flow, Channeling and Connectivity in
350 Heterogeneous Porous Formations. *Mathematical Geosciences*, *44*(2), 133–145.
351 <https://doi.org/10.1007/s11004-011-9365-2>.
- 352 Holzner, M., Morales, V. L., Willmann, M., & Dentz, M. (2015). Intermittent Lagrangian
353 velocities and accelerations in three-dimensional porous medium flow. *Physical Review E -*
354 *Statistical, Nonlinear, and Soft Matter Physics*, *92*(1), 013015.
355 <https://doi.org/10.1103/PhysRevE.92.013015>.
- 356 Hyman, J. D., & Winter, C. L. (2014). Stochastic generation of explicit pore structures by
357 thresholding Gaussian random fields. *Journal of Computational Physics*, *277*, 16–31.
358 <https://doi.org/10.1016/j.jcp.2014.07.046>.
- 359 Hyman, J. D., Smolarkiewicz, P. K., & Winter, C. L. (2012). Heterogeneities of flow in
360 stochastically generated porous media. *Physical Review E*, *86*(5), 056701.
361 <https://doi.org/10.1103/PhysRevE.86.056701>.
- 362 Jiménez-Martínez, J., De Anna, P., Tabuteau, H., Turuban, R., Borgne, T. Le, & Méheust, Y.
363 (2015). Pore-scale mechanisms for the enhancement of mixing in unsaturated porous media
364 and implications for chemical reactions. *Geophysical Research Letters*, *42*(13), 5316–5324.

365 <https://doi.org/10.1002/2015GL064513>.

366 Kang, P. K., De Anna, P., Nunes, J. P., Bijeljic, B., Blunt, M. J. & Juanes, R. (2014). Pore-scale
367 intermittent velocity structure underpinning anomalous transport through 3-D porous media.
368 *Geophysical Research Letters* 41(17), 6184–6190. <http://dx.doi.org/10.1002/2014gl061475>.

369 Knudby, C., & Carrera, J. (2005). On the relationship between indicators of geostatistical, flow
370 and transport connectivity. *Advances in Water Resources*, 28(4), 405–421.
371 <https://doi.org/10.1016/j.advwatres.2004.09.001>.

372 Le Goc, R., Dreuzy, J. De, & Davy, P. (2010). Advances in Water Resources Statistical
373 characteristics of flow as indicators of channeling in heterogeneous porous and fractured
374 media. *Advances in Water Resources*, 33(3), 257–269.
375 <https://doi.org/10.1016/j.advwatres.2009.12.002>.

376 Lindquist, W. B., Venkatarangan, A., Dunsmuir, J., & Wong, T. (2000). Pore and throat size
377 distributions measured from synchrotron X-ray tomographic images of Fontainebleau
378 sandstones. *Journal of Geophysical Research: Solid Earth*, 105(B9), 21509–21527.
379 <https://doi.org/10.1029/2000JB900208>.

380 Math2Market GmbH. (n.d.). GeoDict. Kaiserslautern (Germany).

381 Neuman, S. P., & Di Federico, V. (2003). Multifaceted nature of hydrogeologic scaling and its
382 interpretation. *Reviews of Geophysics*, 41(3), 1014. <https://doi.org/10.1029/2003RG000130>.

383 Neuman, S. P. (2008). Multiscale relationships between fracture length, aperture, density and
384 permeability. *Geophysical Research Letters*, 35(22), L22402.
385 <https://doi.org/10.1029/2008GL035622>.

386 Nissan, A., & Berkowitz, B. (2018). Inertial Effects on Flow and Transport in Heterogeneous
387 Porous Media. *Physical Review Letters*, 120(5), 54504.
388 <https://doi.org/10.1103/PhysRevLett.120.054504>.

389 Renard, P., & Allard, D. (2013). Connectivity metrics for subsurface flow and transport. *Advances*
390 *in Water Resources*, 51, 168–196. <https://doi.org/10.1016/j.advwatres.2011.12.001>

391 Russian, A., Dentz, M., & Gouze, P. (2016). Time domain random walks for hydrodynamic
392 transport in heterogeneous media. *Water Resources Research*, 52, 3309–3323.
393 <https://doi.org/10.1002/2015WR018511>.

394 Siena, M., Riva, M., Hyman, J. D., Winter, C. L., & Guadagnini, A. (2014). Relationship between
395 pore size and velocity probability distributions in stochastically generated porous media.
396 *Physical Review E*, 89(1), 013018. <https://doi.org/10.1103/PhysRevE.89.013018>

397 Silin, D., & Patzek, T. (2006). Pore space morphology analysis using maximal inscribed spheres.
398 *Physica A: Statistical Mechanics and Its Applications*, 371(2), 336–360.
399 <https://doi.org/10.1016/j.physa.2006.04.048>

400 Tartakovsky, A. M., & Neuman, S. P. (2008). Effects of Peclet number on pore-scale mixing and
401 channeling of a tracer and on directional advective porosity. *Geophysical Research Letters*,
402 35(21), 8–11. <https://doi.org/10.1029/2008GL035895>

403 Tukey, J. W. (1977). *Exploratory Data Analysis*. Reading, PA: Addison-Wesley.

404 Zami-Pierre, F., de Loubens, R., Quintard, M., & Davit, Y. (2016). Transition in the Flow of

405 Power-Law Fluids through Isotropic Porous Media. *Physical Review Letters*, 117(7), 074502.
406 <https://doi.org/10.1103/PhysRevLett.117.074502>

407 Zinn, B., & Harvey, C. F. (2003). When good statistical models of aquifer heterogeneity go bad:
408 A comparison of flow, dispersion, and mass transfer in connected and multivariate Gaussian
409 hydraulic conductivity fields. *Water Resources Research*, 39(3).
410 <https://doi.org/10.1029/2001WR001146>

411